

# Design and Development of Coax-Fed Electromagnetically Coupled Stacked Rectangular Patch Antenna for Broad Band Application

Manotosh Biswas<sup>1, \*</sup> and Mausumi Sen<sup>2</sup>

**Abstract**—In this article, a set of closed-form expressions is proposed to predict the resonant frequency, quality factor, input impedance, bandwidth efficiency, directivity and gain for a coax-fed electromagnetically coupled stacked rectangular patch antenna. The computed results obtained with the present model are compared with the experimental and HFSS simulated results. The present model shows less error against the experimental and simulated results.

## 1. INTRODUCTION

Today, microstrip patch antennas are installed in portable wireless equipments, aircraft radomes, missiles, satellites and various radars [1]. Microstrip patch antennas possess many advantages such as low profile, light weight, small volume, and easy implementation. However, due to their resonant behavior, they radiate efficiently only over a narrow band of frequencies, with bandwidths typically only a few percent (about 5%) [2]. Due to this inherent limitation, the patch antenna is the major obstacle that restricts wide applications. Various radars and telecommunication systems employ multiband (broad bandwidth) characteristics. Therefore, the design and development of broad-band techniques are very important to enhance the bandwidth of microstrip antennas.

While maintaining the advantages of conventional single patch microstrip antennas, microstrip antennas of stacked configurations, consisting of one or more conducting patches parasitically coupled to a driven patch, overcome the inherent narrow bandwidth limitation by introducing additional resonances in the frequency range of operation, achieving bandwidths up to 6–20%. In addition, stacked microstrip configurations have achieved higher gains and offer the possibility of dual-frequency operation [3]. Today, the stacked patch antennas are used in radars, mobile, satellites, UHF RFID, MIMO and reconfigurable antennas [3–14]. Thus, the accurate computation of resonant frequency, input impedance, quality factors, bandwidth and gain of stacked patch antenna is very important to install properly in wireless equipments.

Stacked patch antennas have been investigated by several researchers reported in [15–24]. Among them, most of the articles [15–20] are experiment based, and some of the articles [21–23] are based on numerical methods. The useful parameters of a probe-fed electromagnetically coupled stacked rectangular patch antenna (PFEMCSRPA) are computed by numerical techniques [21–23] and also by commercial software [25]. The numerical methods are rigorous and computationally slow. So, they are not suitable for the design oriented interactive computer-aided design (CAD) for the direct synthesis of PFEMCSRPA. The CAD oriented conformal mapping, cavity model and single resonant parallel  $L$ - $C$ - $R$  circuit are ideal for design purpose because it is very simple, easy to analysis, takes less computational time and can be directly applied to the CAD programs.

---

*Received 21 April 2017, Accepted 17 September 2017, Scheduled 14 October 2017*

\* Corresponding author: Manotosh Biswas (mbiswas@ieee.org).

<sup>1</sup> Department of Electronics & Tele-Communication Engineering, Jadavpur University, 188, Raja Subodh Chandra Mullick Road, Kolkata, PIN 700 032, India. <sup>2</sup> Department of Physics, Gobardanga Hindu College, Khanture, 24 PGS (N), India.

To the best of our knowledge, only one article [24] is available in open literature which provides the closed form expressions. However, this model has some drawbacks: (i) the lower cavity is treated as an uncovered patch, but the lower cavity is actually a patch covered with dielectric layer [26]; (ii) the fringing field effect, i.e., the effective patch length  $b_{1eff}$  of lower patch has not been considered, but the fringing field effect very much depends on relative characteristics of substrates and dielectric cover layers [27]; (iii) it considers both the patches with the same ground plane, but the lower patch is treated as ground plane of upper patch [26]; (iv) it studies only the resonant frequency; (v) the design guideline has not been presented for quality factor, efficiency, directivity, gain and input impedance; and (vi) it has not considered the coupling between lower and upper patches.

We have addressed these problems and proposed a simple model based on conformal mapping, cavity model and single resonant parallel  $L$ - $C$ - $R$  circuit to predict accurately the resonant frequency, input impedance, quality factor, efficiency, directivity and gain for a PFEMCSRPA as shown in Fig. 1. This model is very simple, efficient, fast and employs fewer mathematical steps. Microstrip is an old topic. So, we have employed an old theory for developing the present model. Though the present model employs the old theory or model, it is very efficient to overcome the disadvantages of the previous closed form model [24]. This efficient model is capable of predicting accurately above characteristics for wide range of variations of antenna, substrate and superstrate geometric and electrical parameters.

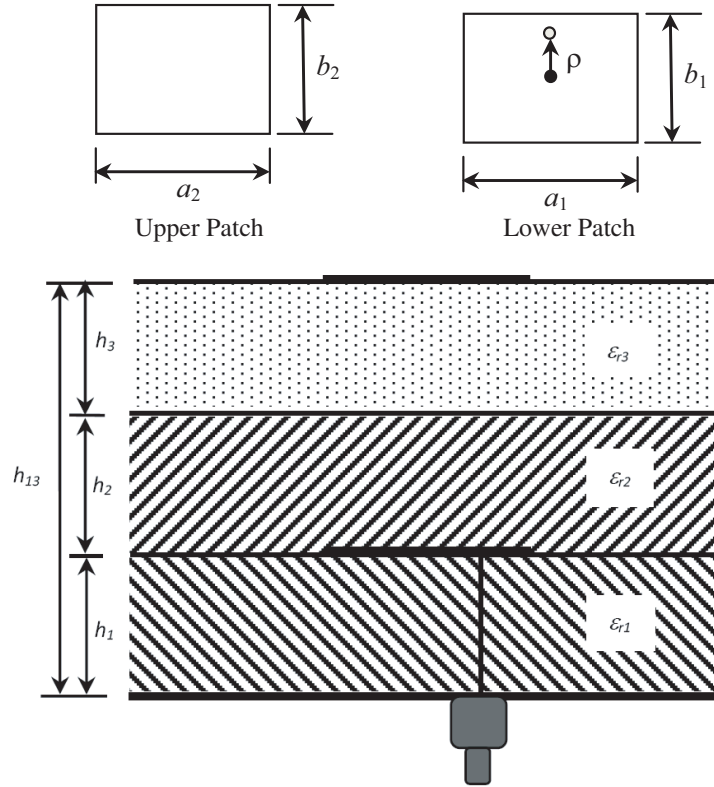


**Figure 1.** Geometry of probe-fed stacked rectangular microstrip patch antenna.

The expressions for this model are introduced in Section 2. Section 3 includes the experimental tests. In Section 4, we present the predicted, measured and simulated results.

## 2. THEORY

The structure under study is shown in Fig. 1, divided into two cavities: lower and upper cavities. The lower patch is termed as a driven patch, and it is excited by a coaxial probe. The upper patch is called a parasitic patch which is not excited by a coaxial probe, but it is electromagnetically coupled with

lower patch. The lower and upper cavities have their own resonances, and they are in parallel [3].

### 2.1. Lower Cavity

The lower cavity is analyzed as a rectangular patch in multi-dielectric layers [26] as shown in Fig. 2.

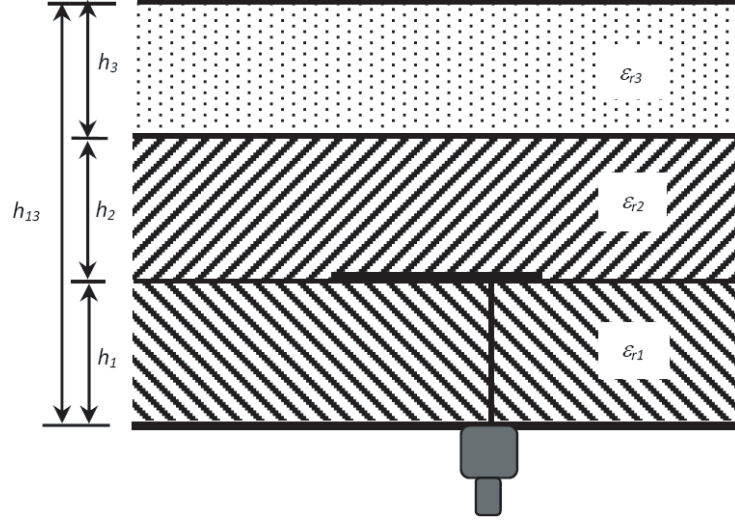


**Figure 2.** Geometry of lower cavity.

#### 2.1.1. Effective Permittivity

When a patch is in multi-dielectric layers, the fringing field between the patch and ground plane is changed, and this effect is accounted for by the effective permittivity  $\epsilon_{r,eff1}$ . The effective permittivity for this structure (Fig. 2) is obtained as [28, 29]:

$$\epsilon_{r,eff1} = \epsilon_{r1} p_{1n} + \epsilon_{r1} (1 - p_{1n})^2 \times \frac{\left[ \epsilon_{r2}^2 p_{2n} p_3 + \epsilon_{r2} \epsilon_{r3} \left\{ p_{2n} p_4 + (p_3 + p_4)^2 \right\} \right]}{\left[ \epsilon_{r2}^2 p_{2n} p_3 p_4 + \epsilon_{r1} (\epsilon_{r2} p_3 + \epsilon_{r3} p_4) (1 - p_{1n} - p_4)^2 \right.} \quad (1)$$

$$\left. + \epsilon_{r2} \epsilon_{r3} p_4 \left\{ p_{2n} p_4 + \{p_3 + p_4\}^2 \right\} \right]$$

where,  $p_{1n}$ ,  $p_{2n}$ ,  $p_3$  and  $p_4$  are the dielectric filling fractions. The derivation of  $\epsilon_{r,eff1}$  and the computational details of these filling fractions are presented in Appendix A.

#### 2.1.2. Effective Patch Length

The effective patch length  $b_{1eff}$  is defined as

$$b_{1eff} = b_1 (1 + q_{b1})^{1/2} \quad (2)$$

here,  $q_{b1}$  is the fringing field factor which strongly depends on the relative characteristics of substrate and superstrates.

The  $q_{b1}$  for this structure is obtained from [30] as

$$q_{b1} = v_1 + v_2 + v_3 + v_4 \quad (3)$$

$$v_1 = 0.882 \frac{h_1}{b_1} \quad (4)$$

$$v_2 = 0.164 \frac{(\epsilon_r - 1) h_1}{\epsilon_r^2 b_1} \quad (5)$$

$$v_3 = \frac{(\epsilon_r + 1) [0.758 + \ln(b_1/h_1 + 1.88)] h_1}{\pi \epsilon_r b_1} \quad (6)$$

$$v_4 = \frac{h_1}{b_1} (0.268\varepsilon_r + 1.65) \quad (7)$$

$$\varepsilon_r = \frac{\varepsilon_{r1}}{\varepsilon_{r,eff1}} \quad (8)$$

### 2.1.3. Resonant Frequency

The dominant mode resonant frequency of a rectangular patch covered with several dielectric layers as shown in Fig. 2 can be expressed by the following formula for conventional geometry [29]:

$$f_{r1} = \frac{c}{2b_{1eff}\sqrt{\varepsilon_{r,eff1}}} \quad (9)$$

where,  $c$  is the velocity of light in free space,  $\varepsilon_{r,eff1}$  the effective permittivity defined in Eq. (1), and  $b_{1eff}$  the effective patch length obtained from Eq. (2).

### 2.1.4. Quality Factor

The total quality factor ( $Q_{T1}$ ) consists of quality factor due to radiation loss  $Q_{r1}$ , quality factor due to dielectric loss  $Q_{d1}$  and quality factor due to conductor loss  $Q_{c1}$ . The  $Q_{T1}$  is defined as

$$Q_{T1} = \left( \frac{1}{Q_{r1}} + \frac{1}{Q_{d1}} + \frac{1}{Q_{c1}} \right)^{-1} \quad (10)$$

The  $Q_{r1}$  is defined as [31]:

$$Q_{r1} = \frac{c\varepsilon_{r1}}{4h_1f_{r1}\varepsilon_{r,eff1}} - \left( \frac{h_{13}}{h_1} \right) \left( \frac{\varepsilon_{r,eff1}}{\varepsilon_{r1}} \right) \quad (11)$$

$$Q_{d1} = \frac{1}{\tan \delta_{e1}} \quad (12)$$

$$\tan \delta_{e1} = \varepsilon_{r1}p_{1n} \tan \delta_1 + \varepsilon_{r2}p_{2n} \tan \delta_2 + \varepsilon_{r3}p_3 \tan \delta_3 \quad (13)$$

$$Q_{c1} = h_1\sqrt{\pi f_{r1}\mu_0\sigma} \quad (14)$$

where,  $\varepsilon_{r,eff1}$  is defined in Eq. (1), and  $f_{r1}$  is obtained from Eq. (9). The computational details of  $p_{1n}$ ,  $p_{2n}$  and  $p_3$  are given by Appendix A.

### 2.1.5. Efficiency, Directivity and Gain

The efficiency ( $\eta_1$ ), Directivity ( $D_1$ ) and gain ( $G_1$ ) can be computed as [3]:

$$\eta_1 = \frac{Q_{T1}}{Q_{r1}} \quad (15)$$

$$D_1 = \frac{4(k_{r1}a_1)^2}{\pi\eta_0G_{S1}} \cos^2 \left[ \frac{\pi(0.5b_1 - \rho)}{b_1} \right] \quad (16)$$

$$G_{S1} = a_1 \frac{7.75 + 2.2(k_{r1}h_1) + 4.8(k_{r1}h_1)^2}{1000\lambda_{r1}} \left\{ 1 + \frac{(\varepsilon_{rr} - 2.45)(k_{r1}h_1)^3}{1.3} \right\} \quad (17)$$

$$G_1 = \eta_1 D_1 \quad (18)$$

The derivation of  $\varepsilon_{rr}$  is provided in Appendix A (A11).

### 2.1.6. Input Impedance

The current through the central conductor of the probe produces an inductive reactance which is in series with the patch reactance itself. The feed reactance  $X_F$  may be obtained from [32] as

$$X_F = \frac{377f_{r1}h_1}{c} \ln \left( \frac{c}{\pi f_{r1}d_0\sqrt{\varepsilon_{rr}}} \right) \quad (19)$$

here,  $d_0$  is probe diameter,  $f_{r1}$  defined in Eq. (9), and the derivation of  $\varepsilon_{rr}$  presented in Eq. (A11) of Appendix A.

Based on the cavity model analysis, the lower rectangular patch can be treated as a resonant cavity modeled by a single resonant parallel  $L_1$ ,  $C_1$  and  $R_1$  circuit as shown in Fig. 3. So, the input impedance seen by a coaxial probe located at a distance  $\rho$  from the centre of the patch is obtained as [33]:

$$Z_{in1} = \frac{R_{in1}}{1 + Q_{T1}^2 B^2} + j \left[ X_F + \frac{R_{in1} Q_{T1} B}{1 + Q_{T1}^2 B^2} \right] \quad (20)$$

where,

$$R_{in1} = R_{r1} \cos^2 \left[ \frac{\pi (0.5b_1 - \rho)}{b_1} \right] \quad (21)$$

$$B = \left[ \frac{f_{r1}}{f} - \frac{f}{f_{r1}} \right] \quad (22)$$

$$R_{r1} = \frac{Q_{T1} h_1}{\pi f_{r1} \varepsilon_{r,eff1} \varepsilon_0 b_1 a_1} \quad (23)$$

where  $\varepsilon_{r,eff1}$  is determined from Eq. (1),  $f_{r1}$  given by Eq. (9), and  $Q_{T1}$  obtained from Eq. (10).

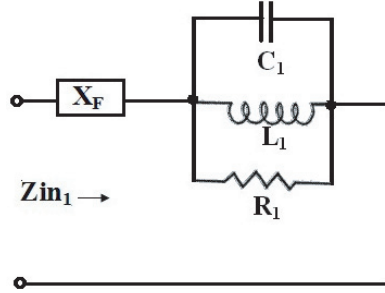


**Figure 3.** Equivalent resonant parallel  $R$ - $L$ - $C$  circuits to calculate the input impedance of lower patch.

## 2.2. Upper Cavity

### 2.2.1. Effective Permittivity

The lower patch is treated as a ground plane of upper patch [26], and the upper patch is analyzed as a rectangular patch on two dielectric layers as shown in Fig. 4. The effective permittivity of this two-layer structure (Fig. 2) is obtained as [34]:

$$\varepsilon_{r,eff2} = \frac{4\varepsilon_{re}\varepsilon_{r,dyn}}{(\sqrt{\varepsilon_{re}} + \sqrt{\varepsilon_{r,dyn}})^2} \quad (24)$$

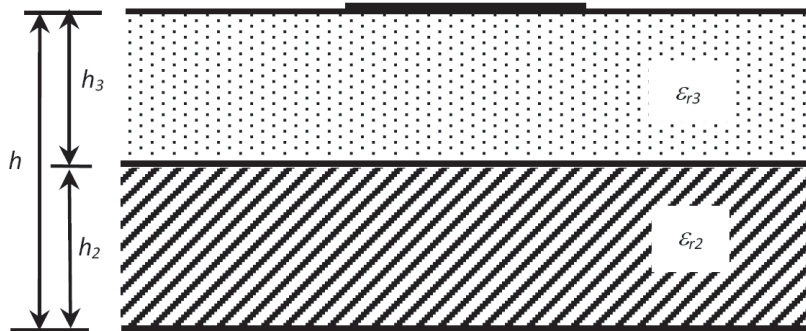


**Figure 4.** Geometry of upper cavity.

here,  $\varepsilon_{re}$  is the equivalent relative permittivity of the medium below the patch, and  $\varepsilon_{r,dyn}$  is dynamic permittivity. The term  $\varepsilon_{r,eff2}$  is introduced to take into account the effect of  $\varepsilon_{re}$ , the equivalent permittivity of the medium below the patch in combination with the dynamic permittivity  $\varepsilon_{r,dyn}$  to improve the model. The computational details of  $\varepsilon_{re}$  and  $\varepsilon_{r,dyn}$  are presented in Appendix B. The sizes of the lower and upper patches may be same or different.

### 2.2.2. Effective Patch Length

The effective patch length for this cavity is obtained as

$$b_{2eff} = b_2 (1 + q_{b2})^{1/2} \quad (25)$$

The derivation of  $q_{b2}$  is presented in Eq. (B13) of Appendix B.

### 2.2.3. Resonant Frequency

The dominant mode resonant frequency for the upper patch is defined as [33]:

$$f_{r2} = \frac{c}{2b_{2eff} \sqrt{\varepsilon_{r,eff2}}} \quad (26)$$

with  $\varepsilon_{r,eff2}$  and  $b_{2eff}$  given by Eqs. (24) and (25), respectively.

### 2.2.4. Quality Factor

The field radiated from the lower patch depends on the lower substrate. A thicker lower substrate will increase the radiated power from the lower patch. A lower patch stops resonating for lower substrate thickness greater than  $0.11\lambda_0$  ( $\varepsilon_{r1} = 2.5$ ). The dielectric constant of lower substrate plays a role similar to that of its thickness. A low value of  $\varepsilon_{r1}$  for the substrate will increase the fringing field at the patch periphery, and thus the radiated power [3]. The fields that radiate from the lower patch are coupled with the upper patch [26]. So, the lower substrate will affect the upper cavity.

$Q_{T2}$  is defined as [26]:

$$Q_{T2} = \frac{h}{h_1} \left( \frac{1}{Q_{r2}} + \frac{1}{Q_{d2}} + \frac{1}{Q_{c2}} \right)^{-1} \quad (27)$$

here  $h/h_1$  represents the coupling factor.

$Q_{r2}$  is defined in [30] as

$$Q_{r2} = \frac{c\sqrt{\varepsilon_{r,eff2}}}{4hf_{r2}} \quad (28)$$

where  $\varepsilon_{r,eff2}$  is defined in Eq. (24), and  $f_{r2}$  is obtained from Eq. (26).

$Q_{d2}$  and  $Q_{c2}$  can be computed as [35]:

$$Q_{d2} = \frac{\pi\sqrt{\varepsilon_{r,eff2}}}{\lambda_{r2}\alpha_d} \quad (29)$$

$$Q_{c2} = \frac{\pi\sqrt{\varepsilon_{r,eff2}}}{\lambda_{r2}(\alpha_c + \alpha_{feed})} \quad (30)$$

here  $\alpha_d$  is the dielectric loss, and  $\alpha_c$  is the conductor loss. The computational details of  $\alpha_d$  and  $\alpha_c$  are available in [36]:

$$\alpha_d = \left( \frac{\varepsilon_{re}}{\varepsilon_{re} - 1} \right) \left( \frac{\varepsilon_{r,eff2} - 1}{\sqrt{\varepsilon_{r,eff2}}} \right) \left( \frac{\tan \delta_{e2}}{\lambda_{r2}} \right) \quad (31)$$

$$\tan \delta_{e2} = \frac{\varepsilon_{r2}h_2 \tan \delta_2 + \varepsilon_{r3}h_3 \tan \delta_3}{h\varepsilon_{re}} \quad (32)$$

$$\alpha_c = \frac{R_S}{Z_r\alpha_2} \quad (33)$$

$$Z_r = \frac{120\pi}{\sqrt{\varepsilon_{r,eff2}}} \left[ \frac{\alpha_2}{h} + 1.393 + 0.667 \ln \left( \frac{\alpha_2}{h} + 1.444 \right) \right]^{-1} \quad (34)$$

$$R_S = \sqrt{\pi f_{r2} \mu_0 / \sigma} \quad (35)$$

$\alpha_{feed}$  is the loss due to the feed, and it can be neglected.  $\varepsilon_{r,eff2}$ ,  $\varepsilon_{re}$  and  $f_{r2}$  are given by Eqs. (24), (B1) and (26), respectively.

### 2.2.5. Efficiency, Directivity and Gain

The efficiency ( $\eta_2$ ), Directivity ( $D_2$ ) and gain ( $G_2$ ) can be computed as [3]:

$$\eta_2 = \frac{Q_{T2}}{Q_{r2}} \quad (36)$$

$$D_2 = \frac{4(k_{r2}a_2)^2}{\pi\eta_0G_{S2}} \cos^2 \left[ \frac{\pi(0.5b_2 - \Gamma)}{b_2} \right] \quad (37)$$

$$G_{S2} = a_2 \frac{7.75 + 2.2(k_{r2}h) + 4.8(k_{r2}h)^2}{1000\lambda_{r2}} \left\{ 1 + \frac{(\varepsilon_{re} - 2.45)(k_{r2}h)^3}{1.3} \right\} \quad (38)$$

$$G_2 = \eta_2 D_2 \quad (39)$$

### 2.2.6. Input Impedance

Like the lower patch, the upper patch is also treated as a resonant cavity modeled by a single resonant parallel  $L_2$ ,  $C_2$  and  $R_2$  circuit as shown in Fig. 5. The input impedance of upper cavity is defined as

$$Z_{in2} = \frac{R_{in2}}{1 + Q_{T2}^2 A^2} + j \left[ \frac{R_{in2} Q_{T2} A}{1 + Q_{T2}^2 A^2} \right] \quad (40)$$

here,

$$R_{in2} = R_{r2} \cos^2 \left[ \frac{\pi(0.5b_2 - \Gamma)}{b_2} \right] \quad (41)$$

$$A = \left[ \frac{f_{r2}}{f} - \frac{f}{f_{r2}} \right] \quad (42)$$

$R_{r2}$  is obtained from [37] as

$$R_{r2} = \frac{2\eta_0 Q_{T2} h}{\pi \sqrt{\varepsilon_{r,eff2}} a_{2eff}} \quad (43)$$

$$a_{2eff} = a_2 (1 + q_{a2})^{1/2} \quad (44)$$

with  $\varepsilon_{r,eff2}$  defined in Eq. (24),  $q_{a2}$  obtained from Eq. (B14), and  $Q_{T2}$  given by Eq. (27).

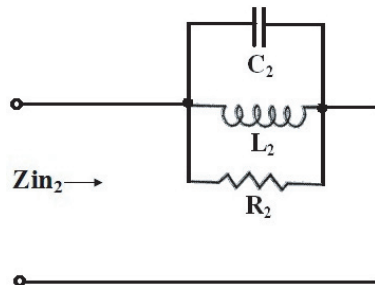


**Figure 5.** Equivalent resonant parallel  $R$ - $L$ - $C$  circuits to calculate the input impedance of upper patch.

### 3. ANTENNA DESIGN AND EXPERIMENTAL TESTS

The prototypes are etched on a Taconic substrate having  $a_1 = a_2 = 30.0$  mm,  $b_1 = b_2 = 30.0$  mm,  $h_1 = h_3 = 0.7875$  mm,  $\epsilon_{r1} = \epsilon_{r3} = 2.33$ ,  $\tan \delta_1 = \tan \delta_3 = 0.001$ . The lower patch is excited with a coaxial probe of diameter  $d = 1.24$  mm located at a distance  $\rho = 8.0$  mm as shown in Fig. 1. To validate the models developed in Section 2, we perform some of the experiments using Network Analyzer Agilent E5071B. The measured resonance is defined as the maximum resistance point. We have previously mentioned in Sections 2.1 and 2.2 that the lower patch is analyzed as a patch covered with multi-dielectric layers, and upper patch is analyzed as a patch without dielectric cover. The effective permittivity of microstrip structure is enhanced, and thus the fringing field effect is decreased for a patch covered with multi-dielectric layers compared to the patch without dielectric cover [28, 29]. Thus, the resonant frequency for a dielectric covered patch antenna is lowered compared to the patch without dielectric cover. So, the lower resonance is treated for lower patch, and upper resonance is considered for upper patch.

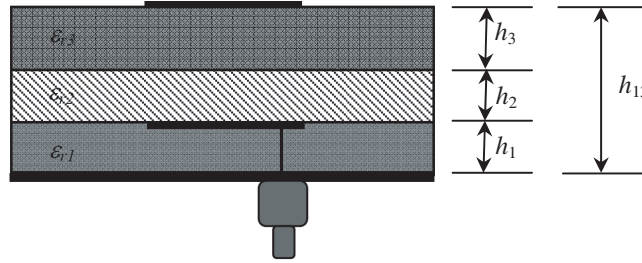
### 4. RESULTS AND DISCUSSIONS

In this section, we present the theoretically predicted, simulated and measured results for the resonant frequency, quality factors, bandwidth, efficiency, directivity, gain and input impedances for this structure.

#### 4.1. Three Layers Structure with Both Driven and Parasitic Patches

In Table 1, we compare the computed resonant frequencies employing the present model with the results of model reported in [24] and HFSS [25] simulation results for different sets of relative permittivities of the layered substrate. The thicknesses of the layers are assumed as  $h_1 = h_2 = h_3 = 0.795$  mm, and the dimensions of both patches are considered to be  $a_1 = a_2 = 45.0$  mm and  $b_1 = b_2 = 37.0$  mm. The errors in results against the HFSS simulation results of the present model are much less than the errors in results of the model reported in [24].

**Table 1.** Comparison of theoretically predicted resonant frequencies and HFSS simulated resonant frequencies for a three-layer stacked rectangular patch antenna with different sets of relative permittivities of the layered substrate.



$\epsilon_{r1}$	$\epsilon_{r2}$	$\epsilon_{r3}$	Resonant frequencies (GHz)					
			HFSS		Computed [24]		Computed [Present]	
			$f_{r1}$	$f_{r2}$	$f_{r1}$	$f_{r2}$	$f_{r1}$	$f_{r2}$
2.2	1.0	2.2	2.575	2.670	2.666	2.721	2.591	2.694
2.2	2.2	2.2	2.530	2.655	2.630	2.721	2.578	2.638
2.5	2.33	2.2	2.415	2.596	2.558	2.559	2.424	2.607
2.62	2.2	2.5	2.360	2.560	2.513	2.502	2.368	2.571
2.62	2.62	2.62	2.330	2.435	2.425	2.502	2.363	2.452
Total average % error					4.793	2.168	0.929	0.618
$a_1 = a_2 = 45.0$ mm, $b_1 = b_2 = 37.0$ mm, $h_1 = h_2 = h_3 = 0.795$ mm								



The computed resonant frequencies employing the present model and the model reported in [24] along with corresponding HFSS resonant frequencies of two patches versus the thickness of the layers are presented in Table 2. The permittivities of the layers are assumed as  $\varepsilon_{r1} = \varepsilon_{r2} = \varepsilon_{r3} = 2.5$ , and the dimensions of both patches are considered to be  $a_1 = a_2 = 45.0$  mm and  $b_1 = b_2 = 37.0$  mm. The errors in results of present model and model in [24] are calculated against HFSS simulation results. The total average error indicates that the present model more accurately computes the resonant frequencies.

**Table 2.** Comparison of theoretically predicted resonant frequencies and HFSS simulated resonant frequencies for a three-layer stacked rectangular patch antenna with different sets of thickness of the layered substrate.

$h_1$ (mm)	$h_2$ (mm)	$h_3$ (mm)	Resonant frequencies (GHz)					
			HFSS		Computed [24]		Computed [Present]	
			$f_{r1}$	$f_{r2}$	$f_{r1}$	$f_{r2}$	$f_{r1}$	$f_{r2}$
0.795	0.000	0.795	2.440	2.520	2.509	2.559	2.432	2.539
1.000	0.508	0.508	2.405	2.510	2.493	2.560	2.389	2.530
1.590	0.795	0.508	2.345	2.495	2.458	2.562	2.312	2.517
2.00	1.590	0.795	2.255	2.450	2.398	2.564	2.265	2.450
3.150	0.508	2.00	2.175	2.420	2.347	2.569	2.150	2.442
Total average % error					5.111	3.407	0.799	0.668
$a_1 = a_2 = 45.0$ mm, $b_1 = b_2 = 37.0$ mm, $\varepsilon_{r1} = \varepsilon_{r2} = \varepsilon_{r3} = 2.5$								

The required frequency separation ( $f_{r2} - f_{r1}$ ) can be obtained by adjusting the parameters and thickness of the layers. Once  $f_{r2}$  and  $f_{r1}$  are determined, the bandwidth can be enlarged considering the center frequency as the matching frequency given by  $f_r = 0.5 \times (f_{r1} + f_{r2})$ . The required frequency separation can also be obtained by adjusting the dimensions of the patches. There is a mutual coupling between the two resonances. The mutual coupling between two resonances is not adjusted by the change of dimensions of the patches, but the substrate thickness and permittivity variation between two resonators adjust the mutual coupling between them resulting in wide bandwidth [3]. Thus, we consider the variation of dielectric structure instead of variation of dimensions of patches.

The computed resistance ( $R$ ) and reactance ( $X$ ) curves employing the present model are compared with HFSS simulated curves in Fig. 6, and very good agreements are observed between them. The parameters for this study are considered as  $a_1 = a_2 = 45.0$  mm,  $b_1 = b_2 = 37.0$  mm,  $h_1 = 1.0$  mm,  $h_2 = h_3 = 0.508$  mm,  $\varepsilon_{r1} = \varepsilon_{r2} = \varepsilon_{r3} = 2.5$ ,  $\tan\delta_1 = \tan\delta_2 = \tan\delta_3 = 0.0025$  and  $\rho = \Gamma = 15.00$  mm.

In Fig. 7 we compare the computed  $R$  and  $X$  curves employing the present model with our experimental curves for two different air dielectric spacings ( $h_2 = 5.0$  mm and 8.0 mm) in between lower patch and the substrate of upper patch. The parameters for this study are taken as  $a_1 = a_2 = 30.0$  mm,  $b_1 = b_2 = 30.0$  mm,  $h_1 = h_3 = 0.7875$  mm,  $\varepsilon_{r1} = \varepsilon_{r3} = 2.33$ ,  $\varepsilon_{r2} = 1.0$ ,  $\tan\delta_1 = \tan\delta_3 = 0.001$ ,  $\tan\delta_2 = 0.000$  and  $\rho = \Gamma = 8.00$  mm.

The comparison between our measured  $R$  and  $X$  curves and computed curves employing the present model for two different PTFE dielectric spacings ( $h_2 = 0.508$  with  $\varepsilon_{r2} = 2.2$  mm and 0.7875 mm with 2.33) in between lower patch and the substrate of upper patch in Fig. 8. The parameters for this study are considered as  $a_1 = a_2 = 30.0$  mm,  $b_1 = b_2 = 30.0$  mm,  $h_1 = h_3 = 0.7875$  mm,  $\varepsilon_{r1} = \varepsilon_{r3} = 2.33$ ,  $\tan\delta_1 = \tan\delta_3 = 0.001$  and  $\rho = \Gamma = 8.00$  mm. The second resonance is disappearing in this case [24].

The structure presented in Section 4.1, which is a three-layer structure and contains two patches, is in stacked configuration, and Section 4.2 represents the two-layer structure with two stacked patches. Both the structures provide dual resonances. The configuration in Section 4.1 provides a large bandwidth and gain compared to the configuration in Section 4.2 [20]. In Section 4.3, only the parasitic patch is printed on two dielectric layers, and driven patch is absent. Section 4.4 represents the structure that contains only the driven patch covered with dielectric layers. The dual resonances are absent for the structures in Sections 4.3 and 4.4. The bandwidth and gain for those structures are less than the

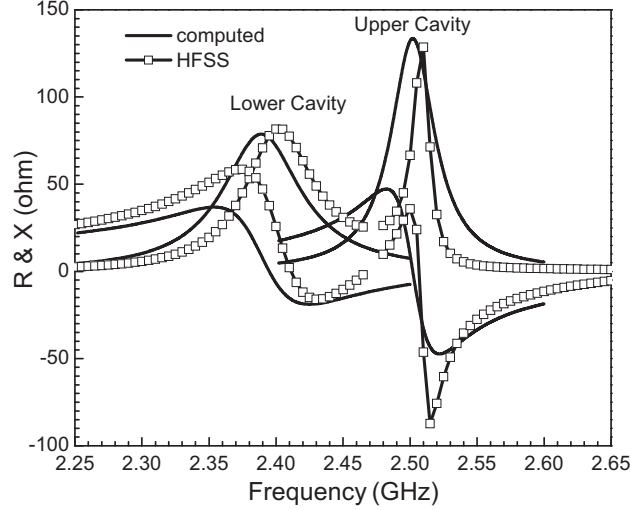


**Figure 6.** Computed and HFSS simulated input impedances for a three-layer stack patch.  $a_1 = a_2 = 45.0$  mm,  $b_1 = b_2 = 37.0$  mm,  $h_1 = 1.0$  mm,  $h_2 = h_3 = 0.508$  mm,  $\epsilon_{r1} = \epsilon_{r2} = \epsilon_{r3} = 2.5$ ,  $\tan \delta_1 = \tan \delta_2 = \tan \delta_3 = 0.0025$ ,  $\rho = \Gamma = 15.00$  mm.

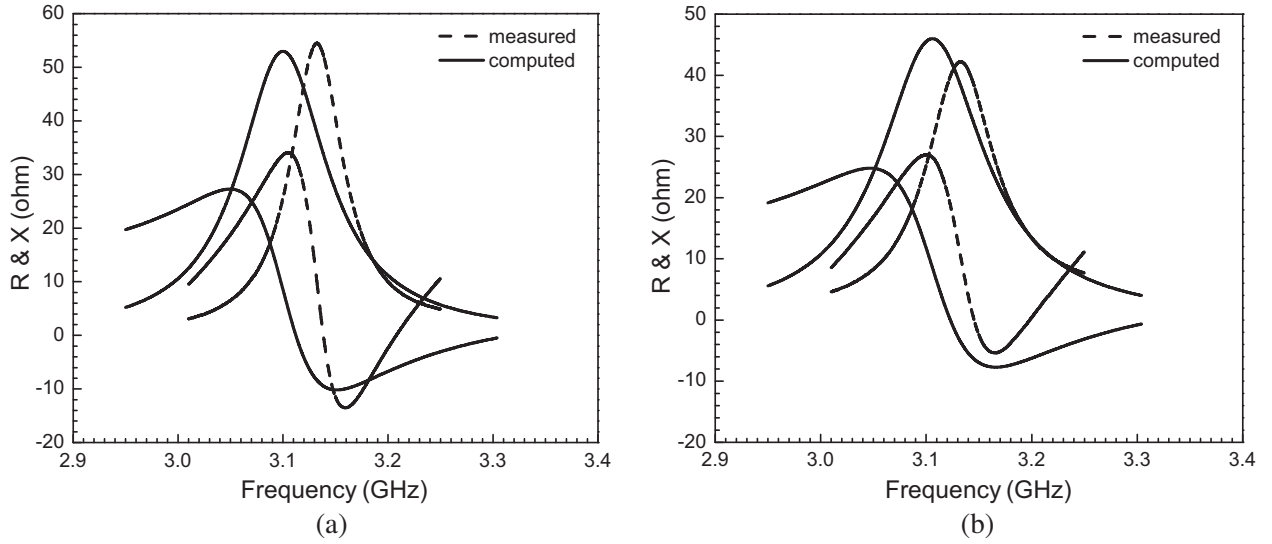


**Figure 7.** Computed and measured input impedances for a three-layer stack patch.  $a_1 = a_2 = 30.0$  mm,  $b_1 = b_2 = 30.0$  mm,  $h_1 = h_3 = 0.7875$  mm,  $\epsilon_{r1} = \epsilon_{r3} = 2.33$ ,  $\epsilon_{r2} = 1.0$ ,  $\tan \delta_1 = \tan \delta_3 = 0.001$ ,  $\tan \delta_2 = 0.000$ ,  $\rho = \Gamma = 8.00$  mm. (a)  $h_2 = 5.0$  mm, (b)  $h_2 = 8.0$  mm.

structures in Sections 4.1 and 4.2. Sections 4.3 and 4.4 are introduced to validate the model developed for a patch covered with dielectric layers and the patch without dielectric layer, respectively. At the end of Section 4.1, we use the same superstrate permittivity as that in Section 4.2 in order to observe the change of lower and upper resonances for the three-layer structure compared to the two-layer structure.

#### 4.2. Two Layers Structure with Both Driven and Parasitic Patches

The computed and HFSS simulated resonant frequencies, efficiencies, directivities, gains and input impedances for lower and upper cavities with the variation of layer thickness are presented in Table 3. The computed values employing the present model agrees well with the simulated ones.

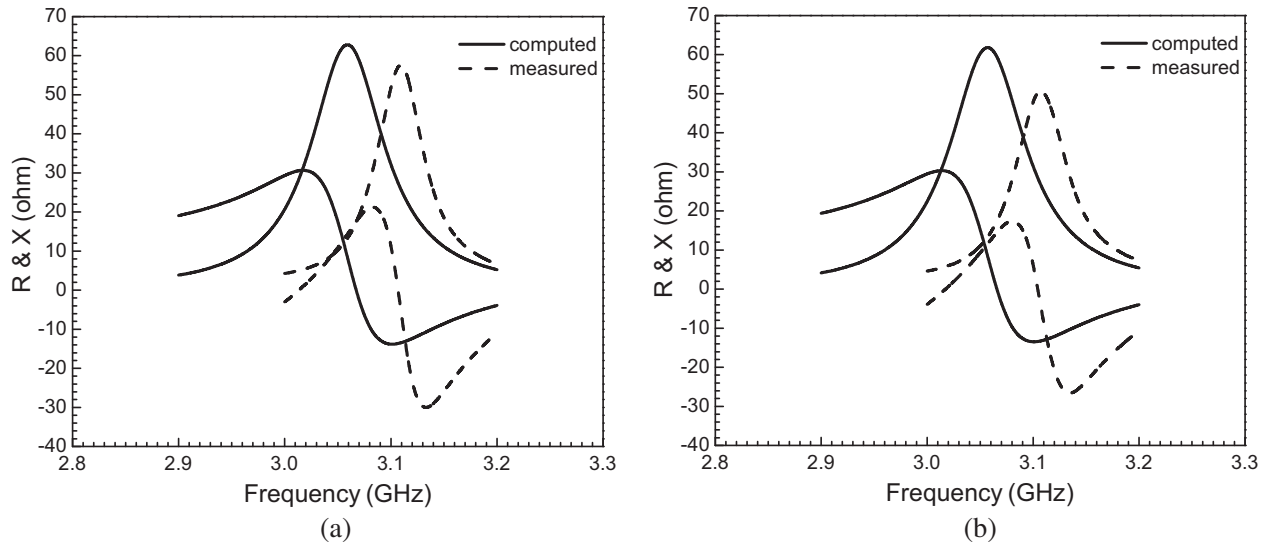
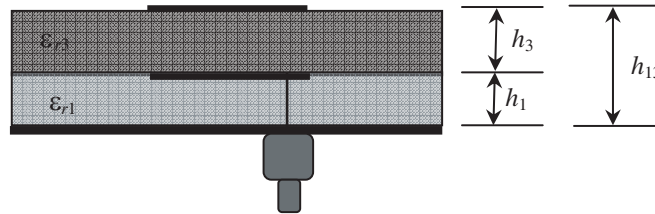


**Figure 8.** Computed and measured input impedances for a three-layer stack patch.  $a_1 = a_2 = 30.0$  mm,  $b_1 = b_2 = 30.0$  mm,  $h_1 = h_3 = 0.7875$  mm,  $\epsilon_{r1} = \epsilon_{r3} = 2.33$ ,  $\tan \delta_1 = \tan \delta_3 = 0.001$ ,  $\rho = \Gamma = 8.00$  mm. (a)  $h_2 = 0.508$  mm,  $\epsilon_{r2} = 2.2$ ,  $\tan \delta_2 = 0.0009$ , (b)  $h_2 = 0.7875$  mm,  $\epsilon_{r2} = 2.33$ ,  $\tan \delta_2 = 0.001$ .

**Table 3.** Comparison of theoretically predicted and HFSS simulated resonant frequencies, input impedances, efficiencies, directivities and gains for a two-layer stacked rectangular patch antenna with different layered thicknesses.



	HFSS	Computed	HFSS	Computed	HFSS	Computed
$f_{r1}$ (GHz)	2.440	2.432	2.32	2.338	2.145	2.193
$f_{r2}$ (GHz)	2.520	2.539	2.485	2.501	2.39	2.393
$R_{r1}$ (ohm)	72.99	75.22	87.07	90.63	91.22	104.4
$R_{r2}$ (ohm)	132.57	126.49	144.0	135.45	149.55	138.14
$\eta_1$ %	73.21	77.43	87.10	88.59	92.82	94.48
$\eta_2$ %	90.13	89.656	94.71	96.75	99.74	98.92
$D_1$ (dB)	7.247	7.526	7.06	7.297	6.524	6.898
$D_2$ (dB)	7.81	7.711	7.83	7.582	7.23	7.252
$G_1$ (dB)	6.33	6.415	6.524	6.771	6.585	6.652
$G_2$ (dB)	7.32	7.237	7.677	7.438	7.21	7.205
	$h_2 = 0.0$ mm, $h_1 = h_3 = 0.795$ mm, $\epsilon_{r2} = 1.0$ , $\epsilon_{r1} = \epsilon_{r3} = 2.5$		$h_2 = 0.0$ mm, $h_1 = h_3 = 1.59$ mm, $\epsilon_{r2} = 1.0$ , $\epsilon_{r1} = \epsilon_{r3} = 2.5$		$h_2 = 0.0$ mm, $h_1 = h_3 = 3.18$ mm, $\epsilon_{r2} = 1.0$ , $\epsilon_{r1} = \epsilon_{r3} = 2.5$	
$a_1 = a_2 = 45.0$ mm, $b_1 = b_2 = 37.0$ mm, $\rho = \Gamma = 15.0$ mm						

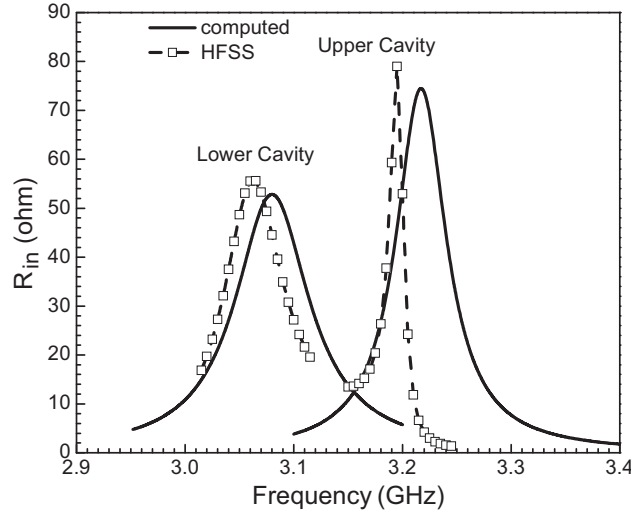


**Figure 9.** Computed and HFSS simulated input resistances for a two-layer stack patch.  $a_1 = a_2 = 30.0$  mm,  $b_1 = b_2 = 30.0$  mm,  $h_1 = h_3 = 0.7875$  mm,  $h_2 = 0.0$  mm,  $\epsilon_{r1} = \epsilon_{r3} = 2.33$ ,  $\epsilon_{r2} = 1.0$ ,  $\tan \delta_1 = \tan \delta_3 = 0.001$ ,  $\tan \delta_2 = 0.000$ ,  $\rho = \Gamma = 7.00$  mm.

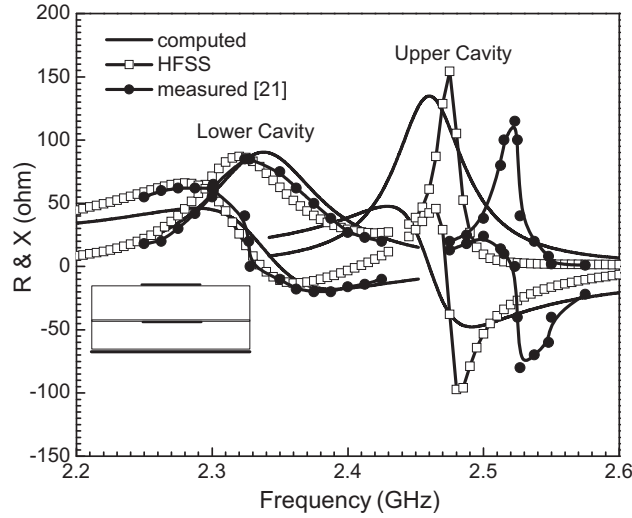


**Figure 10.** Computed, measured and HFSS simulated input impedances for a two-layer stack patch.  $a_1 = a_2 = 45.0$  mm,  $b_1 = b_2 = 37.0$  mm,  $h_2 = 0.0$  mm,  $h_1 = h_3 = 1.59$  mm,  $\epsilon_{r1} = \epsilon_{r3} = 2.5$ ,  $\epsilon_{r2} = 1.0$ ,  $\tan \delta_1 = \tan \delta_3 = 0.0025$ ,  $\tan \delta_2 = 0.000$ ,  $\rho = \Gamma = 15.00$  mm.

In Fig. 9, the computed input resistance curves are compared with the HFSS simulated curves, and close agreement is seen between them. For this study, we consider the parameters as  $a_1 = a_2 = 30.0$  mm,  $b_1 = b_2 = 30.0$  mm,  $h_1 = h_3 = 0.7875$  mm,  $h_2 = 0.0$  mm,  $\epsilon_{r1} = \epsilon_{r3} = 2.33$ ,  $\epsilon_{r2} = 1.0$ ,  $\tan \delta_1 = \tan \delta_3 = 0.001$ ,  $\tan \delta_2 = 0.000$  and  $\rho = \Gamma = 7.00$  mm.

The computed, measured [21] and HFSS simulated input resistance and reactance curves are depicted in Fig. 10. The computed curves agree very well with the HFSS simulated ones. The parameters are taken for this study as  $a_1 = a_2 = 45.0$  mm,  $b_1 = b_2 = 37.0$  mm,  $h_2 = 0.0$  mm,  $h_1 = h_3 = 1.59$  mm,  $\epsilon_{r1} = \epsilon_{r3} = 2.5$ ,  $\epsilon_{r2} = 1.0$ ,  $\tan \delta_1 = \tan \delta_3 = 0.0025$ ,  $\tan \delta_2 = 0.000$  and  $\rho = \Gamma = 15.00$  mm.

The variation of input resistance at resonance as a function of feed location for lower and upper cavities is depicted in Fig. 11. The computed  $R_{in}$  for lower cavity well supports the HFSS simulated results except at the edge because the cavity model does not hold good near the edge of the cavity.

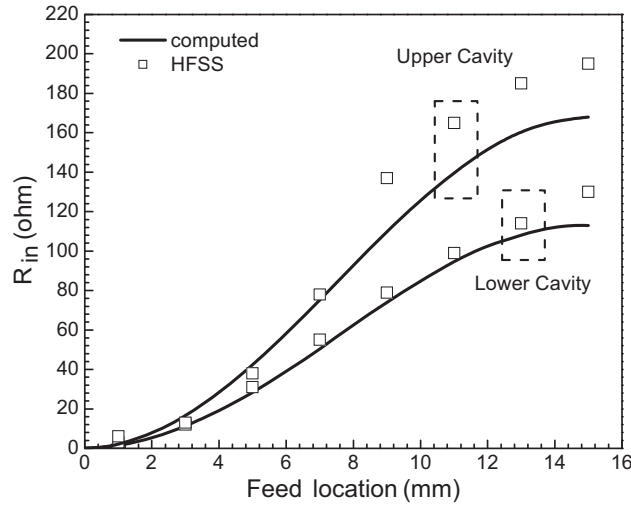


**Figure 11.** Theoretical and HFSS simulation input resistances at resonances as a function of feed location.  $a_1 = a_2 = 30.0$  mm,  $b_1 = b_2 = 30.0$  mm,  $h_1 = h_3 = 0.7875$  mm,  $h_2 = 0.0$  mm,  $\varepsilon_{r1} = \varepsilon_{r3} = 2.33$ ,  $\varepsilon_{r2} = 1.0$ ,  $\tan \delta_1 = \tan \delta_3 = 0.001$ ,  $\tan \delta_2 = 0.000$ .

The discrepancy is observed between the computed and simulated values for the upper cavity. This is because we have assumed that the field radiated by the lower patch is coupled with the upper patch, and a virtual feed location  $\Gamma$  exists.  $\Gamma$  is not an actual feed location point but held as a virtual feed location point.

The discrepancy is observed among the measured, HFSS and theoretical curves in Figs. 7–11. This is due to the following facts: (i) In experimental procedure, a little air gap may be present with the PTFE dielectric spacing or in between lower patch and the substrate of upper patch which cannot be avoided. So, the effective permittivity is changed, and thus the resonant frequency and input impedances are also changed. This fact will introduce errors in the model. (ii) We previously stated that the lower patch behaved as a ground plane of upper patch. So, the lower patch does not provide a large ground plane, and this fact also introduces errors in the model [9]. (iii) The fields radiated by the lower patch are electromagnetically coupled with the upper patch. Some of the fields of lower patch are shared with air, and the rest is electromagnetically coupled with the upper patch. This fact also introduces errors in the model. (iv) The virtual feed location for upper patch also produces error in the model.

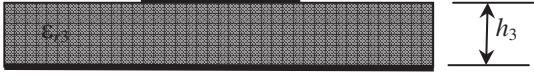
### 4.3. Parasitic Patch with and without Air-Gap and Driven Patch is Absent

In Table 4, we compare the dominant mode resonant frequencies employing the present model and models reported in [38, 39] with the experimental results from [40] for a rectangular patch on a single layer. The total average error shows that the present model more accurately computes the resonant frequencies. In Section 2.1, we have already mentioned that the lower patch behaves as a ground plane of the upper patch. Thus, the lower patch does not behave as the large ground plane for the upper patch. However, here we consider the large ground plane (Appendix B, Fig. B1) for developing the model. So, there is a little discrepancy between the measured and computed values employing the present model.

The computed input resistance and reactance curves employing the present model are compared with our measured curves in Fig. 12, and very good agreement is revealed between them. The parameters for this study are  $a_2 = 30.0$  mm,  $b_2 = 20.0$  mm,  $h_1 = h_2 = 0.0$  mm,  $h_3 = 0.7875$  mm,  $\varepsilon_{r1} = \varepsilon_{r2} = 1.0$ ,  $\varepsilon_{r3} = 2.32$ ,  $\tan \delta_3 = 0.001$  and  $\Gamma = 6.00$  mm.

The variation of resonant frequency and gain as a function of air gap ( $h_2$ ) is presented in Fig. 13. Here we compare the computed curves with the experimental and HFSS simulated results, and very close correlation is observed between them.

**Table 4.** Comparison of experimental dominant mode resonant frequencies from [40] with theoretically predicted values obtained from closed form models presented in [38, 39] and in this work for a rectangular patch.



$a_2$ (mm)	$b_2$ (mm)	$h_3$ (mm)	Resonant Frequency (GHz)			
			Exp. [40]	[38]	[39]	Model
57.0	38.0	3.175	2.31	2.38	2.30	2.38
45.5	30.5	3.175	2.89	2.90	2.79	2.90
29.5	19.5	3.175	4.24	4.34	4.11	4.27
19.5	13.0	3.175	5.84	6.12	5.70	5.90
17.0	11.0	3.175	6.80	7.01	6.47	6.70
14.0	9.0	3.175	7.70	8.19	7.46	7.74
12.0	8.0	3.175	8.27	9.01	8.13	8.40
10.5	7.0	3.175	9.14	9.97	8.89	9.18
9.0	6.0	3.175	10.25	11.18	9.82	10.13
Total Average % Error				5.23	2.88	1.14
Average % Error = [(exp. - theory)/ exp.] $\times$ 100						
$\epsilon_{r3} = 2.33$ , $\epsilon_{r1} = \epsilon_{r2} = 1.0$ , $h_1 = h_2 = 0.0$ mm						

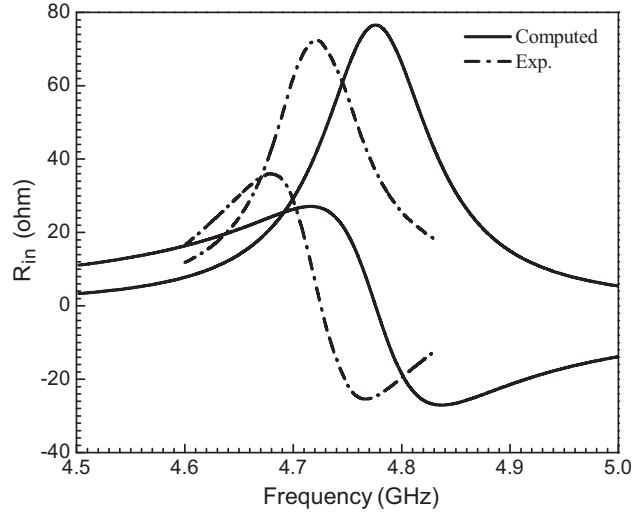


**Figure 12.** Computed and measured input impedances for a rectangular patch on single substrate.  $a_2 = 30.0$  mm,  $b_2 = 20.0$  mm,  $h_1 = h_2 = 0.0$  mm,  $h_3 = 0.7875$  mm,  $\epsilon_{r1} = \epsilon_{r2} = 1.0$ ,  $\epsilon_{r3} = 2.32$ ,  $\tan \delta_3 = 0.001$ ,  $\Gamma = 6.00$  mm.

#### 4.4. Driven Patch with Flush and Spaced Dielectric Superstrates and Parasitic Patch Is Absent

The comparison of the computed resonant frequencies employing the present model and our experimental results for a rectangular patch with spaced dielectric for different  $\epsilon_{r3}$  and  $h_3$  are shown in Table 5. Excellent agreement is observed between them.

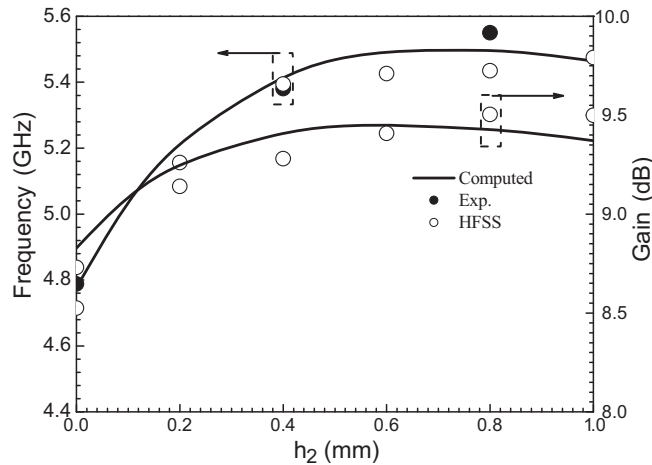
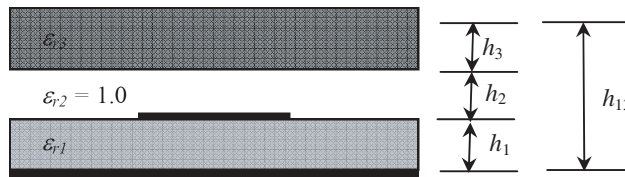


**Figure 13.** Computed, measured and HFSS simulated resonant frequencies and gains for a rectangular patch on the suspended substrate.  $a_2 = 30.0$  mm,  $b_2 = 20.0$  mm,  $h_1 = 0.0$  mm,  $h_2$  is variable,  $h_3 = 0.7875$  mm,  $\epsilon_{r1} = \epsilon_{r2} = 1.0$ ,  $\epsilon_{r3} = 2.32$ .

**Table 5.** Comparison of theoretically predicted and measured resonant frequencies for a rectangular patch with spaced dielectric superstrate for wide range of permittivity ( $\epsilon_{r3}$ ) variation.



$\epsilon_{r3}$	$h_3$ (mm)	Resonant Frequency (GHz)	
		Exp.	Model
2.20	0.508	3.71	3.715
2.32	1.575	3.71	3.717
2.55	2.385	3.72	3.718
2.40	1.580	3.71	3.716
5.00	1.630	3.70	3.695
5.60	1.400	3.69	3.690
9.80	1.630	3.65	3.679
Total Average % Error			0.209
$a_1 = 30.0$ mm, $b_1 = 23.0$ mm, $h_1 = 1.58$ mm, $h_2 = 5.0$ mm, $\epsilon_{r1} = 2.4$ , $\epsilon_{r2} = 1.0$			

In Table 6, we present the computed resonant frequencies employing the present model and the model reported in [41] along with our experimental results for a rectangular patch with flush superstrate for wide range of variation of  $\epsilon_{r3}$ . This comparison shows that the present model is close to the experimental and HFSS simulation results.

**Table 6.** Comparison of theoretically predicted and measured resonant frequencies for a rectangular patch with flush dielectric superstrate for wide range of permittivity ( $\epsilon_{r3}$ ) variation.



$\epsilon_{r3}$	$h_3$ (mm)	Resonant Frequency (GHz)			
		Exp.	HFSS	[41]	Model
2.2	0.508	3.05	3.03	3.09	2.93
2.32	1.575	3.01	2.97	3.09	2.92
2.55	2.385	2.99	2.94	3.08	2.90
5.0	1.630	2.92	2.82	3.07	2.87
5.6	1.400	2.94	2.81	3.08	2.86
9.8	1.630	2.74	2.67	3.07	2.78
$a_1 = 30.0$ mm, $b_1 = 30.0$ mm, $h_1 = 1.58$ mm, $h_2 = 0.0$ mm, $\epsilon_{r1} = 2.4$					
Total average error (%)				4.82*	2.64*
				7.37**	2.32**
* error against exp. and ** error against HFSS					

Figure 14 depicts the comparison of computed input resistance and reactance curves with our experimental curves for a rectangular patch with flush superstrate. The close correlation is seen between them.

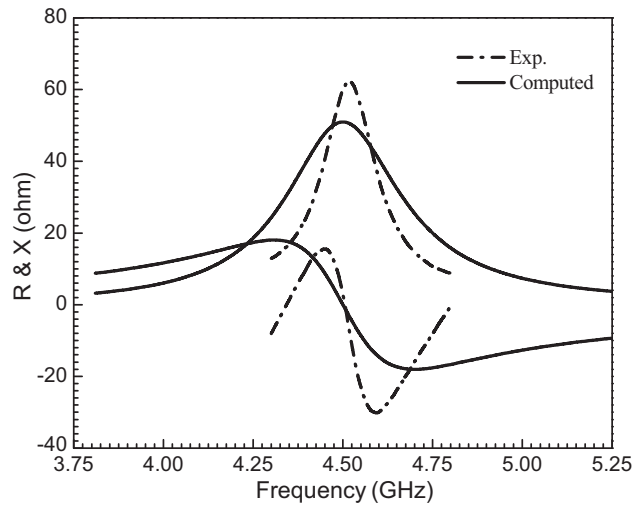


**Figure 14.** Computed and measured input impedances for a rectangular patch with flush superstrate.  $a_1 = 23.0$  mm,  $b_1 = 18.0$  mm,  $h_1 = 1.58$  mm,  $h_2 = 0.0$  mm,  $h_3 = 1.63$  mm,  $\epsilon_{r1} = 2.4$ ,  $\epsilon_{r2} = 1.0$ ,  $\epsilon_{r3} = 5.0$ ,  $\tan \delta_1 = 0.002$ ,  $\tan \delta_2 = 0.000$ ,  $\tan \delta_3 = 0.003$ ,  $\rho = 4.5$  mm.



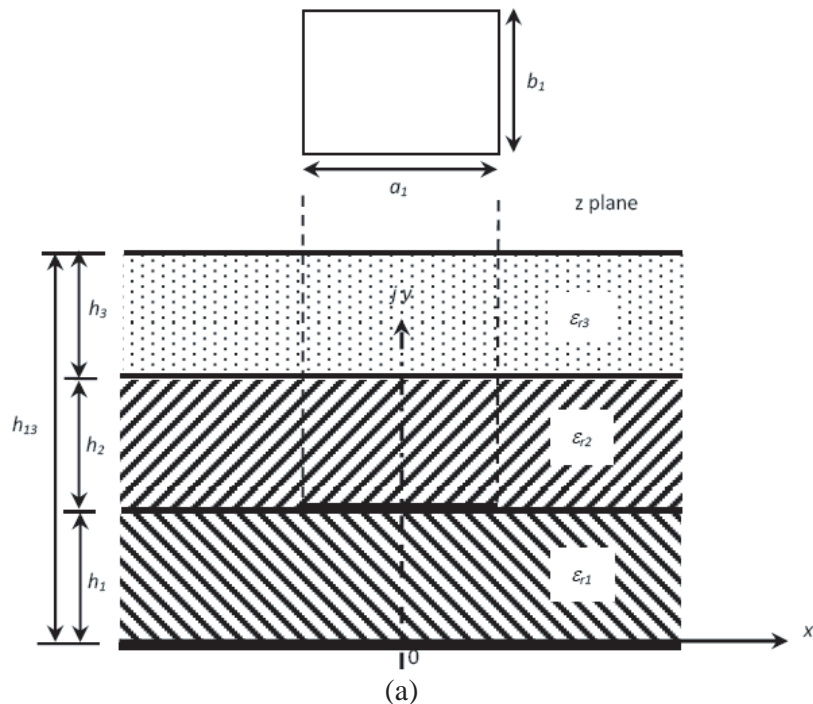
### 5. CONCLUSION

In this article, a simple design guideline is proposed to investigate the resonant frequency, quality factor, bandwidth, efficiency, directivity, gain and input impedance of a stack rectangular patch antenna. The advantages of this model are the mathematical simplicity and low computation cost, and it is faster than the numerical methods and commercially available software. This model is directly applicable to the CAD programs. The computed values are compared with the experimental results available in open literature and our experimental results. We also employ electromagnetic software (HFSS) to generate some results. The present model shows much less error than the experimental and HFSS simulation results. The superiority of the model is that it is also very valid for a rectangular patch on a multilayered substrate and a rectangular patch with flush and spaced dielectric. This model is very useful for practical implementation of a patch on a multilayered substrate, patch with flush and spaced dielectric superstrate and stack rectangular patch antenna in broad band application.

### APPENDIX A. DETERMINATION OF EFFECTIVE PERMITTIVITY ( $\epsilon_{r,eff1}$ ), AND RELATIVE PERMITTIVITY ( $\epsilon_{rr}$ ) OF LOWER CAVITY

The three-layer structure shown in Fig. A1(a) is conformally mapped onto a complex  $g$  plane ( $g = u + jv$ ) with results as shown in Fig. A1(b) based on the method reported in [42] for generalized multilayered microstrip. The filling fraction  $p_i$  is defined as the ratio of each dielectric area  $S_i$  ( $i = 1, 2, 3$ ) to the entire area of the cross section  $S_C$  in the  $g$  plane [43, 44]. The filling fractions  $p_i = S_i/S_C$  for each of these three layers for the wide strip structure ( $a_1/h_1 \geq 1$ ) are defined as [42]

$$p_1 = \frac{S_1}{S_C} = 1 - \frac{\ln\left(\frac{\pi a_{1eff}}{h_1} - 1\right)}{\frac{2a_{1eff}}{h_1}} \tag{A1}$$



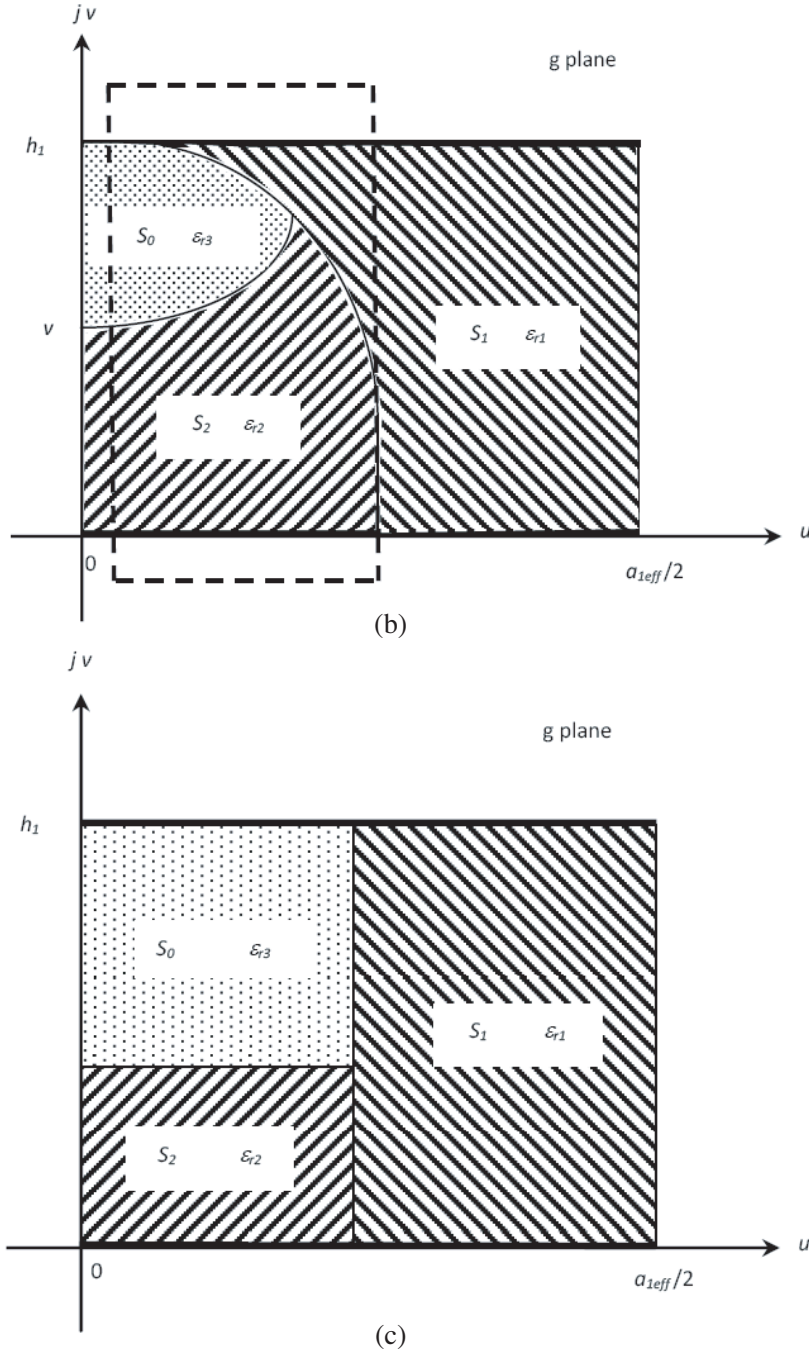


**Figure A1.** (a) Top view and cross-sectional view of the rectangular patch antenna structure under study. (b) Conformally mapped equivalent parallel plate structure with region of note enclosed by the dashed line. (c) Approximate distribution of dielectric materials between parallel plates as presented in [41] and [42].

$$p_2 = \frac{S_2}{SC} = 1 - p_1 - \frac{h_1 - v}{2a_{1eff}} \ln \left[ \pi \frac{a_{1eff}}{h_1} \frac{\cos(\pi v/2h_1)}{\pi \left( \frac{h_{13}}{h_1} - \frac{1}{2} \right) + \frac{v}{2} \frac{\pi}{h_1}} + \sin(\pi v/2h_1) \right] \quad (A2)$$

$$p_3 = \frac{S_3}{S_C} = \frac{h_1 - v}{2a_{1eff}} \ln \left[ \pi \frac{a_{1eff}}{h_1} \frac{\cos(\pi v/2h_1)}{\pi \left( \frac{h_{13}}{h_1} - \frac{1}{2} \right) + \frac{v \pi}{2 h_1}} + \sin(\pi v/2h_1) \right] \quad (A3)$$

$$v = \frac{2h_1}{\pi} \arctan \left[ \frac{\pi}{\frac{\pi a_{1eff}}{2 h_1} - 2} \left( \frac{h_{13}}{h_1} - 1 \right) \right] \quad (A4)$$

The filling fraction expressions developed by [41] and [42] ignore the behavior in the limit when there is no superstrate. In this case,  $h_{13} = h_1$ ,  $v$  in Equation (A4) goes to zero, and  $p_2$  should also go to zero. However,  $p_2$  as given in Eq. (A2), does not go to zero in this limit, indicating that the model developed in both [41] and [42] overestimates the filling fraction of the superstrate in all situations. To rectify this inconsistency, a new filling fraction  $p_3$  equal to half the value of  $p_2$  in the limit when  $h_{13} = h_1$  was reported in [28]:

$$p_4 = \frac{h_1}{2a_{1eff}} \ln \left( \frac{\pi}{2} - \frac{h_1}{2a_{1eff}} \right) \quad (A5)$$

This new filling fraction is used to modify two of the existing filling fractions, with  $p_{1n}$  and  $p_{2n}$  now given by

$$p_{1n} = p_1 - p_4 \quad (A6)$$

$$p_{2n} = 1 - p_{1n} - p_3 - 2p_4 \quad (A7)$$

with  $p_3$  given by Eq. (A3). The term  $a_{1eff}$  present in Eqs. (1A)–(5A) is defined as an effective line width of the lower patch and computed as

$$a_{1eff} = \sqrt{\varepsilon_{rr}/\varepsilon_{r,eff1}} \left[ \left\{ a_1 + 0.882h_1 + 0.164h_1 \frac{(\varepsilon_{rr} - 1)}{(\varepsilon_{rr})^2} \right\} + h_1 \frac{(\varepsilon_{rr} - 1)}{\pi \varepsilon_{rr}} \{ \ln(0.94 + a_1/2h_1) + 1.451 \} \right] \quad (A8)$$

here,  $\varepsilon_{rr}$  is the relative permittivity of an ideal single substrate microstrip structure under consideration, and  $\varepsilon_{r,eff1}$  is the composite effective permittivity of the multilayer structure. In order to compute  $a_{1eff}$ , a two-step iteration is considered starting with an approximation  $\varepsilon_{rr} = \varepsilon_{r1}$  and  $\varepsilon_{r,eff1} = \varepsilon_{rr}$ . Once  $\varepsilon_{r,eff1}$  and  $\varepsilon_{rr}$  are determined using this first value of  $a_{1eff}$ , Eq. (A8) is employed to compute the effective line width a second time.

The distribution and propagation of the electric field lines within the structure under test can be best explained by [28]. As shown in Fig. A2, the electric field flux lines are capable of following three different paths in the structure under study. Path 1 reflects the flux within the substrate of the structure. Path 2 represents the flux that exists strictly in the superstrate and the substrate. Finally, the flux line is extended into the material above the superstrate by path 3. The derivation of effective permittivity,  $\varepsilon_{eff1}$ , of the parallel plate structure visualized in Fig. A3 yields [28]:

$$\varepsilon_{r,eff1} = \varepsilon_{r1} p_{1n} + \varepsilon_{r1} (1 - p_{1n})^2 \quad (A9)$$

$$\times \frac{\left[ \varepsilon_{r2}^2 p_{2n} p_3 + \varepsilon_{r2} \varepsilon_{r3} \left\{ p_{2n} p_4 + (p_3 + p_4)^2 \right\} \right]}{\left[ \varepsilon_{r2}^2 p_{2n} p_3 p_4 + \varepsilon_{r1} (\varepsilon_{r2} p_3 + \varepsilon_{r3} p_4) (1 - p_{1n} - p_4)^2 \right] + \varepsilon_{r2} \varepsilon_{r3} p_4 \left\{ p_{2n} p_4 + \{ p_3 + p_4 \}^2 \right\}} \quad (A10)$$

The computation of effective permittivity of the structure in Fig. A1(a) employing Eq. (9A) allows consideration of the structure as an equivalent microstrip structure with semi-infinite superstrate with relative permittivity equal to unity and a single dielectric substrate with relative permittivity equal to

$$\varepsilon_{rr} = \frac{2\varepsilon_{r,eff1} - 1 + \left( 1 + \frac{10h_1}{a_{1eff}} \right)^{-1/2}}{1 + \left( 1 + \frac{10h_1}{a_{1eff}} \right)^{-1/2}} \quad (A11)$$

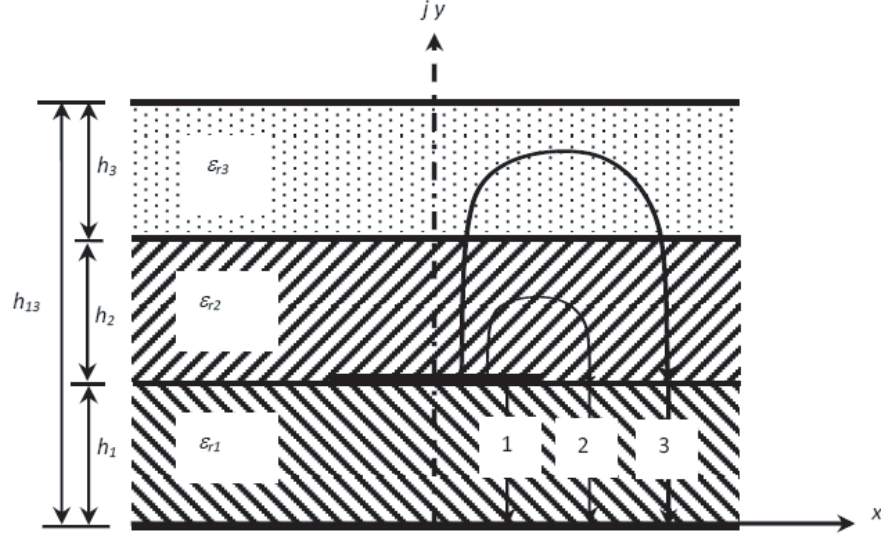


**Figure A2.** Illustration of electric flux paths for the structure shown in Fig. A1(a).

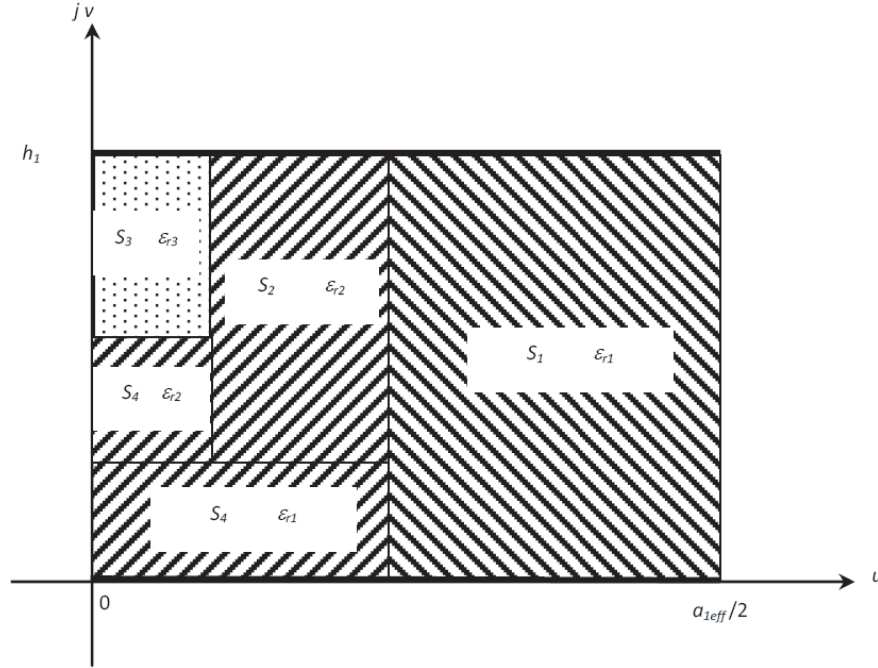


**Figure A3.** Proposed filling fraction arrangement for calculation of effective permittivity that preserves the electric flux paths described in Fig. 2. The region to the extreme right ( $S_1, \epsilon_{r1}$ ) reproduces the capacitive effect of electric flux Path 1. The region containing  $S_2$  ( $\epsilon_{r2}$ ) and a portion of  $S_4$  with relative permittivity equal to  $\epsilon_{r1}$  reproduce the capacitive effect of electric flux Path 2. The remaining region to the extreme left containing  $S_3$  ( $\epsilon_{r3}$ ),  $S_4$  ( $\epsilon_{r2}$ ), and a portion of  $S_4$  with relative permittivity equal to  $\epsilon_{r1}$  reproduces the capacitive effect of electric flux Path 3.

## APPENDIX B. DETERMINATION OF EFFECTIVE PERMITTIVITY ( $\epsilon_{r,eff2}$ ) OF UPPER CAVITY

The rectangular microstrip patch is modeled as a cavity with a magnetic wall along the edge. This is a two-layer cavity (Fig. B1): the upper layer has thickness  $h_3$  with relative permittivity  $\epsilon_{r3}$ , and lower layer has thickness  $h_2$  with permittivity  $\epsilon_{r2}$ . In order to give a general formulation for both the single

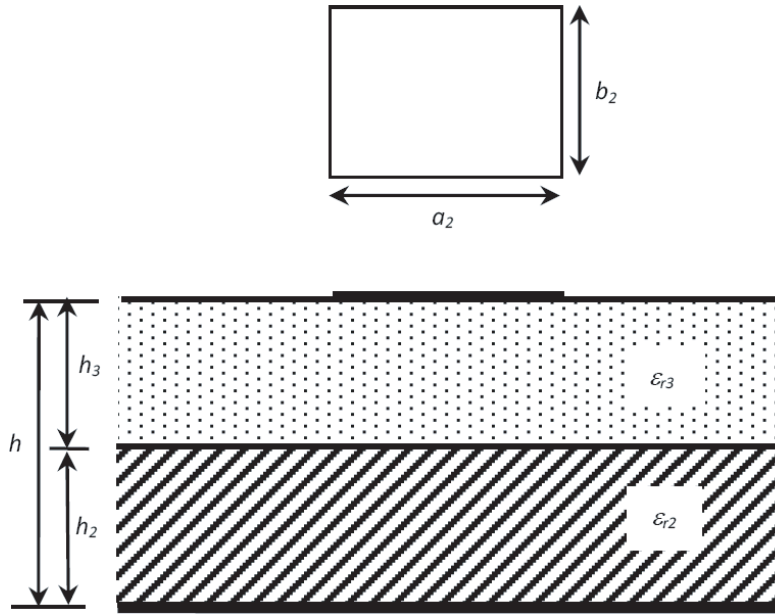


**Figure B1.** Top view and cross-sectional view of the rectangular patch antenna structure under study.

and the two-layer structures, the two-layer structure is modeled as the single-layer one having substrate thickness of  $h = h_3 + h_2$  and an equivalent substrate relative permittivity of  $\epsilon_{re}$  determined under the cavity model approximations as

$$\epsilon_{re} = \frac{\epsilon_{r2}\epsilon_{r3}h}{\epsilon_{r2}h_3 + \epsilon_{r3}h_2} \tag{B1}$$

In order to account for the influence of the fringing field at the edge of the rectangular patch, the term dynamic permittivity is considered. The dynamic permittivity  $\epsilon_{r,dyn}$  depends on the dimensions ( $a_2, b_2, h$ ), equivalent substrate relative permittivity  $\epsilon_{re}$ , and field configuration of the mode under study [45]. It can be expressed as

$$\epsilon_{r,dyn} = \frac{C_{dyn}(\epsilon = \epsilon_0\epsilon_{re})}{C_{dyn}(\epsilon = \epsilon_0)} \tag{B2}$$

In Equation (B2),  $C_{dyn}(\epsilon)$  is the total dynamic capacitance of the condenser formed by the conducting patch and the ground plane separated by a dielectric of permittivity  $\epsilon$ .  $C_{dyn}(\epsilon_0)$  is the total dynamic capacitance when  $\epsilon = \epsilon_0$ . The  $C_{dyn}(\epsilon)$  can be written as

$$C_{dyn}(\epsilon) = C_{o,dyn}(\epsilon) + 2C_{e1,dyn}(\epsilon) + 2C_{e2,dyn}(\epsilon) \tag{B3}$$

where  $C_{o,dyn}$  is the dynamic main field capacitance without considering the fringing field. This can be calculated as

$$C_{o,dyn}(\epsilon) = \frac{\epsilon_0\epsilon_{re}a_2b_2}{h\delta_n\delta_m} = \frac{C_{o,stat}(\epsilon)}{\delta_n\delta_m} \tag{B4}$$

$$C_{o,stat}(\epsilon) = \frac{\epsilon_0\epsilon_{re}a_2b_2}{h} \tag{B5}$$

where,  $C_{o,stat}(\epsilon)$  represents the static main field capacitance without fringing field, and  $\delta_n$  and  $\delta_m$  are in the form

$$\begin{aligned} \delta_i &= 1 & \text{for } i &= 0 \\ &= 2 & \text{for } i &\neq 0 \end{aligned} \tag{B6}$$

Then, a dynamic edge capacitance for each side of the patch taking into account the influence of the fringing field is calculated. The dynamic edge capacitance  $C_{e1,dyn}(\epsilon)$  on one side of patch length  $b_2$

and the dynamic edge capacitance  $C_{e2,dyn}(\varepsilon)$  on one side of patch width  $a_2$  can be computed as

$$C_{e1,dyn}(\varepsilon) = \frac{1}{\delta_n} C_{e1,stat}(\varepsilon) \quad (B7)$$

$$C_{e2,dyn}(\varepsilon) = \frac{1}{\delta_m} C_{e2,stat}(\varepsilon) \quad (B8)$$

where,  $C_{e1,stat}(\varepsilon)$  represents the static edge capacitance on one side of patch length  $b_2$ , and  $C_{e2,stat}(\varepsilon)$  represents the static edge capacitance on one side of patch width  $a_2$ .

The static edge capacitance for a circular disk was reported in [46]. Based on this concept, the static edge capacitance for rectangular patch can be computed as

$$C_e = \frac{\varepsilon_0 \varepsilon_{re} a_2 b_2}{h} (1 + q_{b2} + q_{a2}) \quad (B9)$$

In Eq. (9B), the first term represents the static main capacitance  $C_{o,stat}(\varepsilon)$ , and  $q_{b2}$  and  $q_{a2}$  arise due to the fringing field at the edge of patch length  $b_2$  and patch width  $a_2$ , respectively. Thus,  $C_{e1,stat}(\varepsilon)$  and  $C_{e2,stat}(\varepsilon)$  are defined as

$$C_{e1,stat}(\varepsilon) = 0.5 C_{o,stat}(\varepsilon) q_{b2} \quad (B10)$$

and

$$C_{e2,stat}(\varepsilon) = 0.5 C_{o,stat}(\varepsilon) q_{a2} \quad (B11)$$

$q_{b2}$  and  $q_{a2}$  are the fringing field factors at the edge of the patch length  $b_2$  and at the edge of the patch width  $a_2$ , respectively. The fringing field factor  $q$  at the edge of a circular patch of radius  $r$  was reported in [47] as

$$q = \frac{2h}{\pi r \varepsilon_{re}} \left[ \log\left(\frac{r}{2h}\right) + (1.41\varepsilon_{re} + 1.77) + \frac{h}{r} (0.268\varepsilon_{re} + 1.65) \right] \quad (B12)$$

From Eq. (B12),  $q_{a2}$  and  $q_{b2}$  of the rectangular patch of width  $a_2$  and length  $b_2$  are determined. For computing  $q_{b2}$  and  $q_{a2}$ , an equivalence relation between a rectangular patch and a circular patch is considered. To account for equal static fringing fields, equal circumference is considered as the basis of equivalence, resulting in  $a_2 \approx (\pi - 2)r$  and  $b_2 \approx 2r$  [30]. Thus  $q_{b2}$  and  $q_{a2}$  for this structure are obtained as

$$q_{b2} = \frac{1.273h}{b_2 \varepsilon_{re}} \left[ \log\left(\frac{b_2}{4h}\right) + (1.41\varepsilon_{re} + 1.77) + \frac{2h}{b_2} (0.268\varepsilon_{re} + 1.65) \right] \quad (B13)$$

$$q_{a2} = \frac{0.727h}{a_2 \varepsilon_{re}} \left[ \log\left(\frac{a_2}{2.284h}\right) + (1.41\varepsilon_{re} + 1.77) + \frac{1.142h}{a_2} (0.268\varepsilon_{re} + 1.65) \right] \quad (B14)$$

Now we define the effective permittivity of upper patch as [34]:

$$\varepsilon_{r,eff2} = \frac{4\varepsilon_{re}\varepsilon_{r,dyn}}{(\sqrt{\varepsilon_{re}} + \sqrt{\varepsilon_{r,dyn}})^2} \quad (B15)$$

## REFERENCES

1. Kumar, G. and K. P. Ray, *Broadband Microstrip Antennas*, Artech House, London, 2003.
2. Carver, K. R. and J. W. Mink, "Microstrip antenna technology," *IEEE Trans. Antennas Propagat.*, Vol. 29, 2–23, Jan. 1981.
3. Garg, R., P. Bhartia, I. Bahl, and A. Ittipiboon, *Microstrip Antenna Design Handbook*, Artech House, Canton, MA, 2001.
4. Waterhouse, R. B., *Printed Antennas for Wireless Communications*, John Wiley & Sons, England, 2007.
5. Jin, Y. and Z. Du, "Broadband dual-polarized F-probe fed stacked patch antenna for base stations," *IEEE Antennas Wireless Propagate. Lett.*, Vol. 14, 1121–1124, 2015.
6. Zhu, Q., S. Yang, and Z. Chen, "Modified corner-fed dual-polarised stacked patch antenna for micro-base station applications," *Electro. Lett.*, Vol. 51, 604–606, Apr. 2015.

7. Ali, M., T. M. Sayem, and V. K. Kunda, "A reconfigurable stacked microstrip patch antenna for satellite and terrestrial links," *IEEE Trans. Vehic. Technol.*, Vol. 56, 426–435, Mar. 2007.
8. Zhou, Y., C.-C. Chen, and J. L. Volakis, "Dual band proximity-fed stacked patch antenna for tri-band GPS applications," *IEEE Trans. Antennas Propagat.*, Vol. 55, 220–223, Jan. 2007.
9. Wang, Z., S. Fang, S. Fu, and S. Lv, "Dual-band probe-fed stacked patch antenna for GNSS applications," *IEEE Antennas Wireless Propagate. Lett.*, Vol. 8, 100–103, 2009.
10. Li, D., P. Guo, Q. Dai, and Y. Fu, "Broadband capacitively coupled stacked patch antenna for GNSS applications," *IEEE Antennas Wireless Propagate. Lett.*, Vol. 11, 701–704, 2012.
11. Falade, O. P., M. U. Rehman, Y. Gao, X. Chen, and C. G. Parini, "Single feed stacked patch circular polarized antenna for triple band GPS receivers," *IEEE Trans. Antennas Propagat.*, Vol. 60, 4479–4484, Oct. 2012.
12. Wang, Z., S. Fang, S. Fu, and S. Jia, "Single-fed broadband circularly polarized stacked patch antenna with horizontally meandered strip for universal UHF RFID applications," *IEEE Trans. Micro. Theory Tech.*, Vol. 59, 1066–1073, Apr. 2011.
13. Gao, Y., R. Ma, Y. Wang, Q. Zhang, and C. Parini, "Stacked patch antenna with dual-polarization and low mutual coupling for massive MIMO," *IEEE Trans. Antennas Propagat.*, Vol. 64, 4544–4549, Oct. 2016.
14. Hu, J., Z.-C. Hao, and W. Hong, "Design of a wideband quad-polarization reconfigurable patch antenna array using a stacked structure," *IEEE Trans. Antennas Propagat.*, Vol. 65, 3014–3023, Jun. 2017.
15. Tiwari, H. and M. V. Kartikeyan, "A stacked microstrip patch antenna with fractal shaped defects," *Progress In Electromagnetics Research C*, Vol. 14, 185–195, 2010.
16. Ghorbani, K. and R. B. Waterhouse, "Dual polarized wide-band aperture stacked patch antennas," *IEEE Trans. Antennas Propagat.*, Vol. 52, 2171–2174, Aug. 2004.
17. Anguera, J., C. Puente, and C. Borja, "A procedure to design stacked microstrip patch antennas based on a simple network model," *Micro. Opt. Technol. Lett.*, Vol. 30, 149–151, Aug. 2001.
18. Anguera, J., C. Puente, C. Borja, N. Delbene, and J. Soler, "Dual-frequency broad-band stacked microstrip patch antenna," *IEEE Antennas Wireless Propagate. Lett.*, Vol. 2, 36–39, 2003.
19. Jang, W.-G. and J.-H. Choi, "Design of a wide and multiband aperture-stacked patch antenna with reflector," *Micro. Opt. Technol. Lett.*, Vol. 49, 2822–2824, Nov. 2007.
20. Lee, R. Q. and K. F. Lee, "Experimental study of the two-layer electromagnetically coupled rectangular patch antenna," *IEEE Trans. Antennas Propagat.*, Vol. 38, 1298–1302, Aug. 1990.
21. Hassani, H. R. and D. M. Syahkal, "Study of electromagnetically coupled stacked rectangular patch antennas," *IEE Proc. — Micro. Antennas Propagat.*, Vol. 142, 7–13, Feb. 1995.
22. Waterhouse, R. B., "Design of probe-fed stacked patches," *IEEE Trans. Antennas Propagat.*, Vol. 47, 1780–1784, Dec. 1999.
23. Reineix, A. and B. Jecko, "Analysis of microstrip patch antennas using finite difference time domain method," *IEEE Trans. Antennas Propagat.*, Vol. 31, 381–390, Mar. 1991.
24. Liu, Z.-F., P.-S. Kooi, L.-W. Li, M.-S. Leong, and T.-S. Yeo, "A method for designing broad-band microstrip antennas in multilayered planar structure," *IEEE Trans. Antennas Propagat.*, Vol. 47, 1416–1420, Sep. 1999.
25. HFSS 13: Ansoft's Corp.
26. Tagle, J. G. and C. G. Christodoulou, "Extended cavity model analysis of stacked microstrip ring antennas," *IEEE Trans. Antennas Propagat.*, Vol. 45, 1626–1635, Nov. 1997.
27. Alexopoulos, N. G. and D. R. Jackson, "Fundamental superstrate (cover) effects on printed circuit antennas," *IEEE Trans. Antennas Propagat.*, Vol. 32, 807–816, Aug. 1984.
28. Bernhard, J. T. and C. J. Tousignant, "Resonant frequencies of rectangular microstrip antennas with flush and spaced dielectric superstrates," *IEEE Trans. Antennas Propagat.*, Vol. 47, 302–308, Feb. 1999.
29. Biswas, M. and M. Sen, "Design and development of rectangular patch antenna with superstrates for the application in portable wireless equipments and aircraft radome," *Micro. Opt. Technol.*

- Letts.*, Vol. 56, 883–893, Apr. 2014.
30. James, J. R. and P. S. Hall, *Handbook of Microstrip Antennas*, Peter Peregrinus, London, U.K., 1989.
  31. Biswas, M. and A. Mandal, “Experimental and theoretical investigation to predict the effect of superstrate on the impedance, bandwidth, and gain characteristics for a rectangular patch antenna,” *Journal of Electromagnetic Waves and Applications*, Vol. 29, No. 16, 2093–2109, 2015.
  32. Deshpande, M. and M. Bailey, “Input impedance of microstrip antennas,” *IEEE Trans. Antennas Propagat.*, Vol. 30, 645–650, Jul. 1982.
  33. Abboud, F., J. P. Damiano, and A. Papiernik, “Simple model for the input impedance of coax-fed rectangular microstrip patch antenna for CAD,” *IEE Proc.*, Vol. 135, Pt. H, 323–326, Oct. 1988.
  34. Chattopadhyay, S., M. Biswas, J. Y. Siddiqui, and D. Guha, “Rectangular microstrips with variable air gap and varying aspect ratio: Improved formulations and experiments,” *Micro. Opt. Technol. Lett.*, Vol. 51, No. 1, 169–173, Jan. 2009.
  35. Verma, A. K. and Nasimuddin, “Resonance frequency and bandwidth of rectangular microstrip antenna on thick substrate,” *IEEE Micro. Wireless Comp. Lett.*, Vol. 12, 60–62, Feb. 2002.
  36. Pozar, D. M., *Microwave Engineering*, John Wiley & Sons, Inc., Hoboken, New Jersey, 2012.
  37. Khellaf, A., D. Thouroude, and J. P. Daniel, “Simple expression of rectangular patch’s resistance at resonance,” *Electron. Lett.*, Vol. 26, 1188–1190, Jul. 1990.
  38. Hammerstad, E. O., “Equations for microstrip circuit design,” *Proc. 5th European Micro. Conf.*, 268–272, Hamburg, Sep. 1975.
  39. James, J. R., P. S. Hall, and C. Wood, *Microstrip Antenna — Theory and Design*, Peter Peregrinus, London, U.K., 1981.
  40. Chang, E., S. A. Long, and W. F. Richards, “Experimental investigation of electrically thick rectangular microstrip antennas,” *IEEE Trans. Antennas Propagat.*, Vol. 34, 767–772, Jun. 1986.
  41. Zhong, S.-S., G. Liu, and G. Qasim, “Closed form expressions for resonant frequency of rectangular patch antennas with multi dielectric layers,” *IEEE Trans. Antennas Propagat.*, Vol. 42, 1360–1363, Sept. 1994.
  42. Svačina, J., “Analysis of multilayer microstrip lines by a conformal mapping method,” *IEEE Trans. Microwave Theory Tech.*, Vol. 40, 769–772, Apr. 1992.
  43. Wheeler, H., “Transmission-line properties of parallel wide strips by a conformal mapping approximation,” *IEEE Trans. Microw. Theory Tech.*, Vol. 12, 280–289, Mar. 1964.
  44. Wheeler, H. A., “Transmission-line properties of parallel strips separated by a dielectric sheet,” *IEEE Trans. Microwave Theory Tech.*, Vol. 13, 172–185, Mar. 1965.
  45. Wolff, I. and N. Knoppik, “Rectangular and circular microstrip disk capacitors and resonators,” *IEEE Trans. Micro. Theory Tech.*, Vol. 22, 857–864, Oct. 1974.
  46. Wheeler, H. A., “A simple formula for the capacitance of a disc on dielectric on a plane,” *IEEE Trans. Micro. Theory Tech.*, Vol. 30, 2050–2054, Nov. 1982.
  47. Chew, W. C. and J. A. Kong, “Effects of fringing field on the capacitance of circular microstrip disk,” *IEEE Trans. Micro. Theory Tech.*, Vol. 28, 98–104, Feb. 1980.